THESIS FOR THE DEGREE OF LICENTIATE OF ENGINEERING

Atom Probe Tomography of Hydrogen and of Grain Boundaries in Corroded Zircaloy-2

GUSTAV SUNDELL

Department of Applied Physics

CHALMERS UNIVERSITY OF TECHNOLOGY

Gothenburg, Sweden 2012

Atom Probe Tomography of Hydrogen and of Grain Boundaries in Corroded Zircaloy-2
GUSTAV SUNDELL

Department of Applied Physics
Chalmers University of Technology
SE-412 96 Gothenburg
Sweden
Telephone + 46 (0)31-772 1000

Cover:
APT reconstruction of the metal-oxide interface region in corroded Zircaloy-2. The image shows segregation of Fe (purple) and Ni (green) to grain boundaries in the metal (orange) and oxide (blue). Each dot represents the position of the different individual atoms in the analyzed sample. The size of the two boxes is 50x50x140 nm^3.

Printed by:
Chalmers Reproservice
Gothenburg, Sweden 2012

Atom probe tomography of hydrogen and of grain boundaries in corroded Ziracloy-2

Gustav Sundell
Department of Applied Physics
Chalmers University of Technology

Abstract

Due to their low thermal neutron capture cross-section, zirconium alloys are widely used in the nuclear industry for fuel cladding and structural components. The lifetime of the fuel assemblies in the reactors are largely dictated by the ability of the fuel cladding to withstand corrosion and mechanical damage. The waterside corrosion mechanism of zirconium alloys is closely related to another material degradation process, namely hydrogen pick-up.

In order to study the hydrogenation of zirconium on the atomic level, atom probe tomography (APT) is utilized. This technique offers some unique virtues for nanometer scale materials analysis, such as equal sensitivity to all elements. However, as APT has rarely been used for hydrogen studies previously, methods for accurate quantitative analysis need to be developed.

The vacuum chamber in which APT analysis is carried out typically contains small amounts of residual gases, e.g. hydrogen. Hydrogen gas can be adsorbed onto the APT specimen, and analyzed along with the specimen material. This will obscure the true hydrogen content that is found in subsequent data evaluation.

A study of the experimental parameters that govern hydrogen adsorption has been carried out on a nickel-based alloy. Hydrogen adsorption can be reduced significantly by field evaporation either at low field strengths, using high laser pulse energies, or at very high field strengths using voltage pulsing. Supply of hydrogen to the tip apex is concluded to occur by direct gas phase adsorption, and it resides on the surface in a field-adsorbed state. It will then be desorbed through field evaporation, where the field strength in the tip vicinity will determine whether it is detected in atomic ion or molecular ion form.

The metal-oxide interface in corroded Zircaloy-2 was also studied using APT. Segregation of the alloying elements Fe and Ni to deformation-induced sub-grain boundaries in the metal was observed. The chemistry of these grain boundaries is subsequently inherited by the oxide as the metal is consumed. This is concluded to be of importance for the corrosion and hydrogen-pickup kinetics, as oxide grain boundaries may act as transport paths for oxygen and hydrogen.

Keywords: Atom probe tomography, Hydrogen pick-up, Hydrogen analysis, corrosion, Zirconium alloys, Field adsorption.

Preface

The research work in this thesis was carried out at the Materials Microstructure Division at the Department of Applied Physics, Chalmers University of Technology, Göteborg, Sweden, during the period October 2010 to November 2012, under supervision of Professor Hans-Olof Andrén and co-supervision by Dr Mattias Thuvander.

List of appended papers

I. *Hydrogen analysis in APT: methods to control adsorption and dissociation of H_2*
G. Sundell, M. Thuvander and H.-O. Andrén
In review for *Ultramicroscopy*

II. Enrichment of Fe and Ni at metal and oxide grain boundaries in corroded Zircaloy-2
G. Sundell, M. Thuvander and H.-O. Andrén
Corrosion Science, Vol. 65, 2012, pp. 10-12

I wrote both papers and did all the experimental work.

I also contributed to the following papers:

I. *Atom probe tomography of Oxide Scales*
K. Stiller, L. Viskari, G. Sundell, F. Liu, M. Thuvander, H.-O. Andrén, D. J. Larson, T. Prosa, D. Reinhard
Accepted for *Oxidation of Metals*

II. *Towards a comprehensive mechanistic understanding of hydrogen uptake in zirconium alloys by combining atom probe analysis with electronic structure calculations*
M. Lindgren, G. Sundell, I. Panas, L. Hallstadius, M. Thuvander, H.-O. Andrén
Submitted to *Zirconium in the Nuclear Industry 17th Int. Symp,* ASTM

I did the APT work on zirconium and contributed to authoring paper I, and did the APT work and co-authored paper II.

TABLE OF CONTENTS

1. Introduction

1.1 Background

Perhaps the most important challenge that science and engineering face in the 21st century is to satisfy the rising energy demand in the world. Rapid economic growth in developing countries calls for improved standards of living, accommodated partly by increased electricity and fuel consumption. At the same time, consciousness of the devastating effects of climate change, caused by emission of greenhouse gases into the atmosphere, is emerging. This has led to a surge of interest in renewable sources of energy over the past decades, such as photovoltaics, wind power and biomass combustion.

While some of these techniques show great promise, renewable sources of energy are still far from being capable of replacing fossil fuels. This has brought renewed interest in nuclear power for electricity generation. Nuclear power has the advantage of producing significantly less carbon dioxide than fossil fuel combustion processes. New generations of nuclear plants offer substantial improvements in terms of efficiency as well as safety. This has prompted many governments to expand their nuclear industries, and many countries are now constructing new Generation III-type plants. Today, more than 25 new reactors are in construction only in China [1]. Big research projects are carried out across the world to develop new Generation IV technologies for nuclear power, which will see further improvements in thermal efficiency and fuel usage. The vast majority of reactors in operation today, however, are of type Generation II. Generation II reactor were first taken into operation in the 1950s, but commercial usage did not start until the late 1960s. Continuous improvements to the design have been made since, which has prolonged the lifetime of these early reactor types.

The efficiency of a nuclear plant is limited mainly by the temperature of the coolant in the reactor. Higher coolant temperatures increase the available amount of work that can be extracted form a system, in accordance with Carnot's theorem. Another factor that can be improved is increasing the burn-up of the reactor fuel. Higher burn-ups increase the total energy output of the fuel, and, crucially, means that the number of the spent fuel assemblies decreases. The longer the fuel stays in the reactor, the less harmful material is left to dispose of when the fuel cycles are ended. Such enhancements of the nuclear plant performance put severe strains on the structural materials in the reactor. The components have to withstand heavy radiation doses as well as an intensely corrosive environment during their time of operation. This requires resilient mechanical properties in combination with good corrosion resistance.

Zirconium alloys were selected at an early stage for usage in nuclear reactor cores, as the low neutron capture cross-section of zirconium prevents it from

interfering with the neutron flux. They are currently utilized as fuel cladding as well as minor structural parts in the core. Two of the main limiting factors for the lifetime of the fuel cladding are the oxidation and the hydrogen pick-up, which are consequences of the waterside corrosion process in the reactor. Hydrogen pick-up causes serious embrittlement of the alloy and damages its advantageous corrosion properties.
Despite several decades of research, the mechanism of hydrogen pick-up in zirconium alloys is yet to be fully understood. Many empirical studies have been carried out on the subject, and new alloys have been developed based on a trial-and-error approach of varying heat treatments and additions of alloying elements.

In order to ultimately address the problem of hydrogenation of zirconium alloys, a mechanistic understanding of the fundamental principles that govern hydrogen uptake is needed.

1.2 Aim of this study

This work is performed as part of the MUZIC-2 program, which is a collaborative project between industry and a number of universities, aimed at elucidating the mechanisms that govern hydrogen uptake in zirconium alloys. The experimental work at Chalmers is focused on atom probe tomography analysis of fuel cladding materials.

The objectives of this study are:

- Investigate the possibility to perform quantitative hydrogen analysis using atom probe tomography.

- Develop methods to perform microanalysis of the regions that are of importance for corrosion and hydriding of zirconium alloys.

- Study the chemical composition of the metal-oxide interface in corroded Zircaloy-2.

- Utilize the knowledge gained from atom probe analysis to formulate a hypothesis for hydrogen pick-up.

2. Zirconium in the nuclear industry

2.1 Nuclear reactors

In a nuclear reactor controlled nuclear fission reactions take place, which generates heat through a series of nuclear chain reactions. Heat from the fission process is passed on to a coolant, typically water, which is used to produce steam that runs through a steam turbine to produce electric power that can be utilized for power distribution or propulsion. Fission is initiated and sustained by a neutron flux, which must be controlled during operation. Neutron flux in the reactor is regulated by the insertion of control rods into the reactor core, and in light water reactor (LWR) designs also by a moderator coolant that reduces the speed of the neutrons. Various designs exist in terms moderator, fuel and coolant. In Swedish nuclear plants, only LWR are used where fast neutrons are slowed down in the fluid to become thermal neutrons, and thereby triggering further fission.

Two types of LWR reactors are in operation in Sweden; pressurized water reactors (PWR) and boiling water reactors (BWR). In PWRs the coolant is kept in liquid state at high pressures (usually around 150 bar [2]) in the reactor core, and passes on thermal energy to a secondary water circuit in a steam generator. A pressurizer regulates pressure in the loop, by adjusting the temperature of the coolant with electrical heaters. A vertical temperature gradient is present along the fuel bundles where the temperature at the bottom is around 275 °C, and the water is heated to 315 °C at the top [3]. In BWRs the water is brought to boil in the core and the electricity generation in the turbine occurs in the primary water circuit. BWRs operate at a significantly lower pressure (around 75 bar) than PWRs, which means that the boiling point of the coolant is reduced to about 285 °C [4]. A schematic illustration of a boiling water reactor is presented in Figure 2.1.

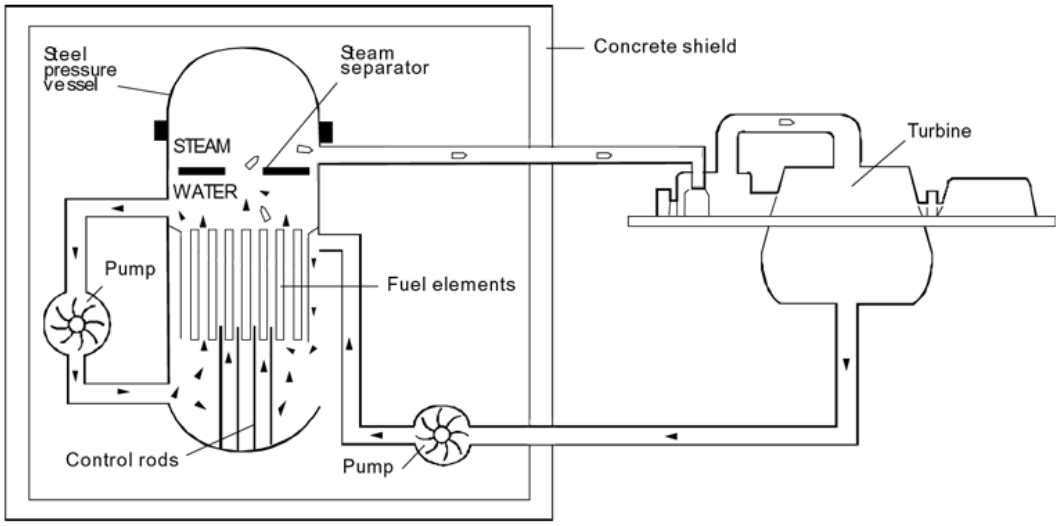

Figure 2.1: Schematics of a boiling water reactor [1].

The fuel in the Swedish reactors comprises pellets of uranium dioxide, which is enriched in the fissionable U-235 isotope. The pellets are inserted into zirconium alloy cladding tubes of approximately 10 mm in diameter. The interior of the tube is sealed and pressurized with helium to reduce potential pellet-cladding interaction and improve thermal conductivity.

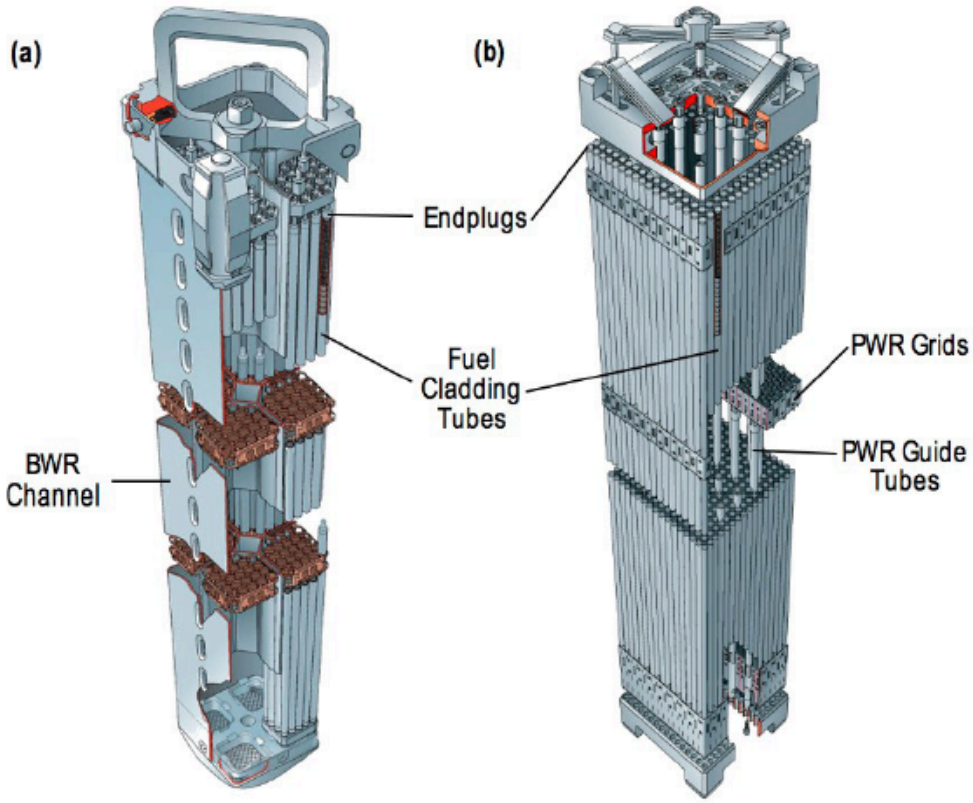

Figure 2.2: BWR (left) and PWR (right) fuel assemblies (courtesy of Westinghouse Electric Sweden AB).

Tubes are grouped together in bundles called fuel assemblies. BWR fuel assemblies are each enclosed in a box to ensure water and steam flow stability. Control rods, fabricated out of highly neutron-absorbing material, can be inserted in the fuel assemblies to regulate the neutron flux in the reactor.
BWR and PWR fuel assemblies are presented in Figure 2.2.

2.2 Fuel cladding alloys

The aggressive environment in the reactor puts extreme requirements on the fuel cladding material. It has to withstand fission products from the inside and water at temperatures ranging from 280-350°C at the outer surface [4]. In addition it must not only be able to cope with neutron irradiation but also interfere as little as possible with the neutron flux, in order to maintain high neutron efficiency in the reactor. Zirconium has a very low thermal neutron capture cross-section, which means that it is nearly transparent for low energy neutrons that have high probability of causing fission of the fuel. This quickly made it an attractive candidate for usage in early nuclear reactor cores. Pure zirconium, however, has relatively poor corrosion resistance and insufficient mechanical strength for usage in structural components. Experiments with Sn addition led to the development Zircaloy-1 for early BWR, and this alloy was soon abandoned in favor of Zircaloy-2. This alloy contains small amounts of Fe, Cr and Ni in addition to Sn, which significantly improved corrosion resistance. Zircaloy-2 is still in wide use in BWR reactors, although French manufacturers use some Nb containing alloys.

PWR reactors has seen a larger number of alloys, but the most common in Europe today are ZIRLO™ (Sn, Nb, Fe), M5™ (Nb) and Zircaloy-4 (Sn, Fe, Cr).
Graphite-moderated RBMK reactors in Russia and heavy-water moderated CANDU reactors in Canada primarily use binary Zr-Nb alloys.

Table 1: Some common Zr alloys for nuclear applications and their alloying elements. Secondary phase particles (SPPs) found in the materials are also given.

Alloy		Nominal content (wt%)						
	Usage	Sn	Fe	Ni	Nb	Cr	O	SPPs
Zircaloy-2	BWR, CANDU	1,2-1,7	0,07-0,20	0,03-0,08	-	0,05-0,15	0,125	$Zr(Fe,Cr)_2$ - $Zr_2(Fe,Ni)$
Zircaloy-4	BWR, PWR, CANDU	1,2-1,7	0,18-0,24	-	-	0,07-0,13	0,125	$Zr(Fe,Cr)_2$
M5	PWR	-	<500 ppm	-	0,8-1,2	-	0,125	β-Nb - $Zr(Nb,Fe)_2$
Zr-2.5 Nb	CANDU, RBMK	-	-	-	2,4-2,8	-	0,125	Nb enriched β-Zr (metastable)
ZIRLO	PWR	1,0-1,1	0,09-0,10	-	1,0-1,2	-	0,125	β-Nb - $(Zr,Nb)_2Fe$

In general, these alloys contain small amounts of trace elements of Si, P and C. Their solubility in α-zirconium is very low and they form small precipitates. The exact role of these particles has not been clearly established.

2.3 Microstructure and heat treatments

Pure solid zirconium exists in two phases; a hexagonal close-packed structure (hcp) at ambient temperature (α-zirconium), and a body centered cubic structure at temperatures above 865°C (β-zirconium) [4]. Thus the relevant crystal structure for all nuclear applications is the α-phase. Lattice parameters are a = 0.323 nm and c = 0.515 nm which means that it is slightly compressed in the c-direction with respect to the ideal hcp structure. A hexagonal unit cell is shown in Figure 2.3.

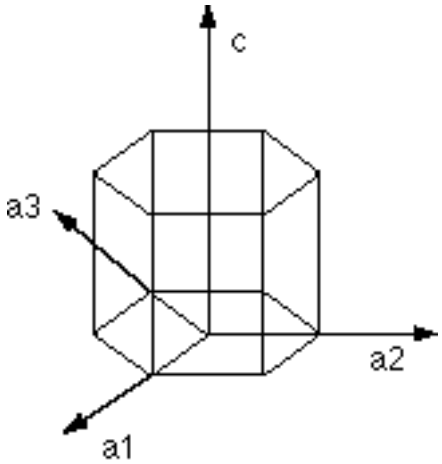

Figure 2.3: Hexagonal unit cell.

Prolonged neutron irradiation leads to growth in the basal plane and compression in the c-direction [5]. The hexagonal crystal structure gives the α-phase strongly anisotropic properties that must be accounted for in fuel cladding processing.

Zirconium alloys for nuclear applications are typically subjected to the following thermomechanical processing steps [4]:

- Hot forging in the β-phase at temperatures around 1000 °C. This dissolves all second phase particles (SPPs) and gives rise to significant grain growth. Billets or slabs are formed.
- Water quenching from the β-phase at a temperature above 1000 °C. Upon quenching the β-grains undergo a bainitic or martensitic transformation to form α-lamellae. Alloying elements such as Fe, Cr and Ni are rejected by the α-front and precipitate as SPPs at the boundaries of the lamellae.
- Upper α-phase extrusion to form tubes (temperature 575-725°C.).
- A number of cold rollings and subsequent anneals in vacuum at intermediate temperature (550-600 °C). Deformation of up to 80% is achieved where the final annealing leads to either a stress relieved (Zircaloy-4 cladding tubes) or a fully recrystallized state (Zircaloy-2 cladding tubes).

The resulting recrystallized microstructure in Zircaloy-2 is highly textured with equiaxed grains. A characteristic pole figure for tube material is shown in Figure 2.4.

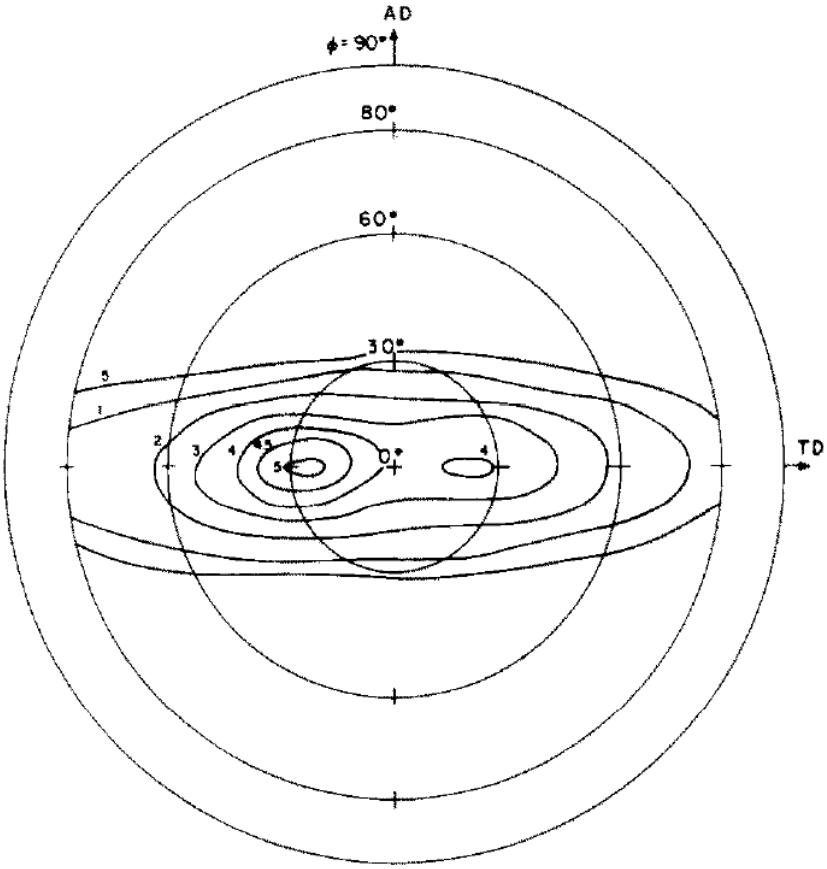

Figure 2.4: (0002) pole figure from Zircaloy-2. AD indicates the rolling direction (axial direction of the tube) and TD indicates the transverse direction (circumferential direction of the tube) [6].

The <c> axes lies in a plane perpendicular to the tube axis, often some 30 degrees from the radial direction (see Figure 4), which improves the yield stress and makes the tubes more resistant to internal pressure [5].

The size and distribution of SPPs are strongly dependent on the cold rolling and annealing steps. This has led to some development work of heat treatments over the years in order to obtain optimal properties with regards to creep resistance and corrosion.

3. Corrosion behavior

3.1 Overview

One of the main limiting factors for the lifetime of zirconium fuel cladding tubes is corrosion. As a result of this the oxidation properties of zirconium alloys have been studied rather extensively since the first commercial nuclear plants were taken into operation in the 1960's. The native oxide that forms on Zr is monoclinic ZrO_2. The Zr-O phase diagram in presented in Figure 3.1. In ZrO_2 diffusion of oxygen is much faster than diffusion of Zr, which means that the oxide grows inwards and the rate-limiting step is the supply of oxygen to the metal [7]. The oxidation stems from water splitting at an oxide-water interface and has the overall corrosion reaction

$$Zr + 2\,H_2O \rightarrow ZrO_2 + 2H_2$$

The Pilling-Bedworth ratio is 1.55 [8], causing a volume expansion that can only be accommodated by first deforming the underlying metal, and eventually cracking of the oxide.

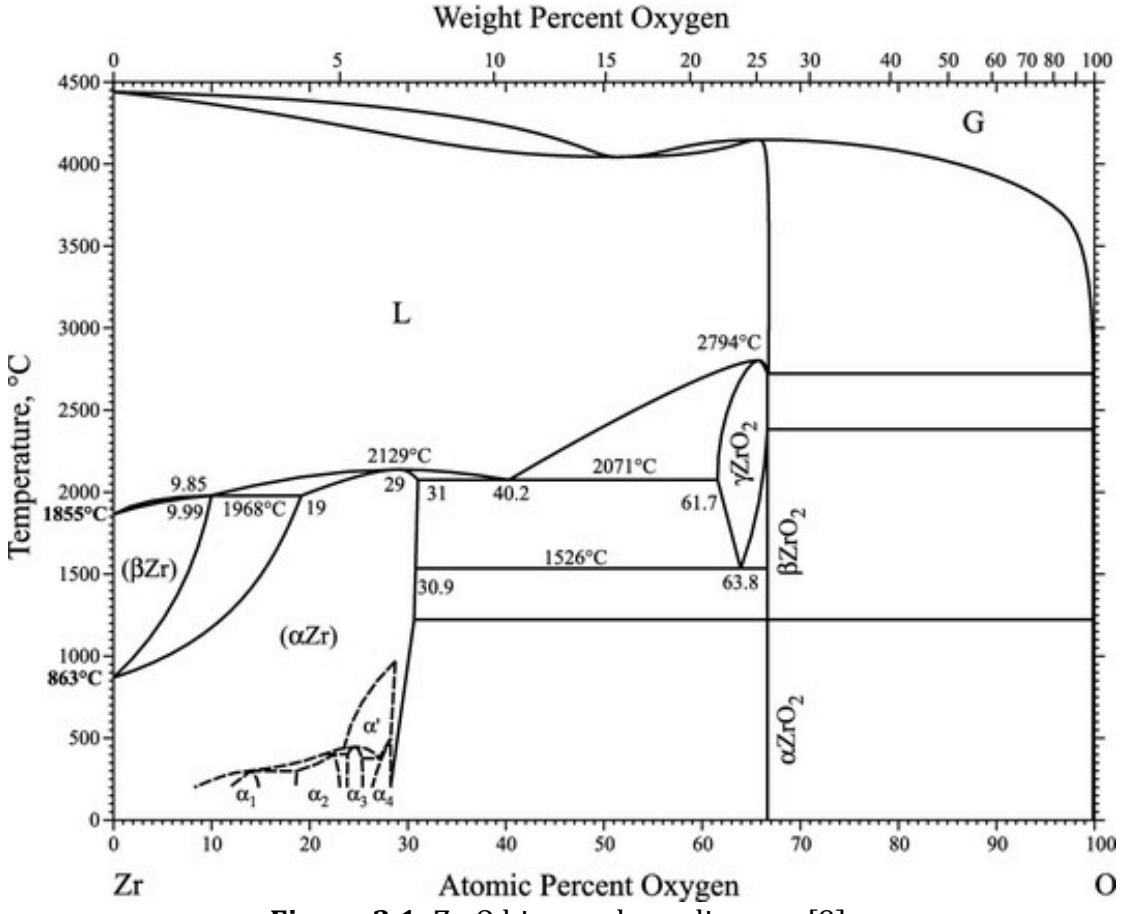

Figure 3.1: Zr-O binary phase diagram [9].

Unlike most structural materials, α-Zr has a rather high solubility of oxygen. At relevant temperatures for nuclear applications the solubility is approximately 29 at% [9]. Diffusion of oxygen in the metal is slower than in the oxide scale, which prevents oxygen saturation in the metal except for in the outermost regions.

3.2 Oxide Growth

The time dependence of the thickness of the ZrO_2 layer growing on top of a Zr alloy is normally described as t^n where n is typically smaller than 0.5. This growth rate stabilizes and collapses in a characteristic cyclic pattern (see Figure 3.2). Firstly a protective oxide is rapidly formed, slowing down the growth significantly. The appearance of the oxide is blackish at this stage, and grains are small and equiaxed [4]. Compressive stresses are high which leads to transformation of some monoclinic oxide to the high-pressure tetragonal oxide phase [10]. Upon further oxidation, monoclinic oxide with columnar morphology develops. The column axes are perpendicular to the metal-oxide interface and have a width of approximately 25 nm. The metal-oxide interface has a wavy morphology, which typically undulates with an amplitude of a few hundred nanometers for thinner oxides [11]. Various theories regarding the origin of these waves exist such as faster O^{2-} diffusion through some oxide column grain boundaries [12], and SPP influence [13].

The protective oxide is stable up to a thickness of approximately 1.5-3 μm, depending on alloy and oxidation conditions, after which it breaks up and a rapid increase in growth rate occurs. This change in oxidation rate is referred to as transition and this phenomenon has been studied extensively [14-16]. At this point, the fraction of tetragonal phase in the oxide decreases sharply. Larger columnar grains that are elongated in a direction normal to the metal-oxide interface replace the small equiaxed grains [17].

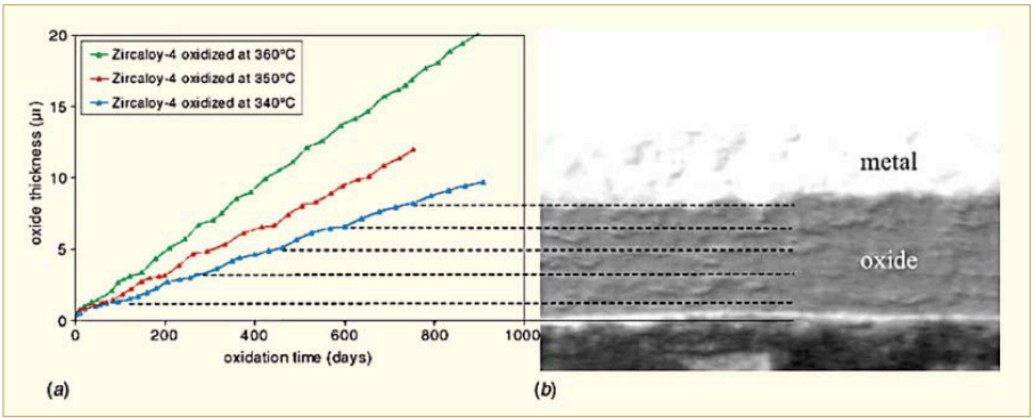

Figure 3.2: Cyclic growth rate of oxide scale on Zircaloy-4. Transitions are associated with cracks in the oxide [18].

These cycles of protective barrier oxide build-up, followed by collapse and rapid growth is repeated numerous times up until thicknesses of several tens, or even hundreds, of micrometers. Eventually a breakaway corrosion stage occurs, where the oxide offers no protection as large cracks and spallation will allow easy access for the water to the metal-oxide interface [4]. Fuel bundles are removed from the reactor well in time before breakaway corrosion occurs.
The rate-limiting step is oxygen diffusion from an oxide-water interface. The exact mechanism for oxygen diffusion through the oxide is not fully known. The early notion that oxygen moves through the oxide lattice by a vacancy mechanism has largely been abandoned and it is now widely accepted that grain boundary diffusion is the most important process [12, 14]. In addition to the uniform corrosion, Zr alloys in BWR reactors may also suffer nodular corrosion. This comprises nucleation of "blisters" of oxide that is associated with rapid growth and rupture of the uniform protective oxide. The problem of nodular corrosion is believed to be connected to large SPPs and has to a large extent been overcome by reducing SPP size [19].

3.3 Influence of alloying elements

Subtle differences in alloying elements can have an enormous impact for the corrosion behavior of the alloy [20]. What is true for fuel cladding in BWR may not necessarily be applicable in PWR plants. Tin is added to virtually all LWR claddings, mainly for mechanical properties as it increases the yield strength of the alloy [4]. It is an α-stabilizer for Zr and is also known to stabilize the tetragonal ZrO_2 phase during corrosion [16]. Sn is fully soluble in the metal matrix as well as in the oxide, and does not form precipitates in commercial alloys. It has long been thought to improve the corrosion resistance [4]. However, this has turned out to be true only for BWR reactors. In PWR alloys the trend in recent years is instead to reduce the Sn content [21]. Examples of this are Optimized ZIRLO™ and low Sn Zircaloy-4.

Niobium is known to delay transition [22]. However it appears that Nb-containing alloys oxidize faster in water vapor than the Nb-free Zircaloys. Nb diffuses very slowly in Zr, making the annealing time during the heat treatment very important. The Zr matrix is typically supersaturated with Nb, which can lead to in-reactor precipitation of fine particles [23].

Iron appears to have a very large impact on the corrosion resistance of Zr alloys. In Zircaloy-2 it forms precipitates with Cr and Ni, but is also to some extent soluble in the matrix [24]. This solubility has been subject to some discussion and its importance for the corrosion properties is debated [13, 25]. The Fe-containing precipitates are more noble than Zr and they start to oxidize at some distance away from the metal-oxide interface [15]. During this process Fe will diffuse out of the particle and form agglomerates of nearly pure iron oxide [26].
Chromium has a very low solubility in the Zr matrix and is only observed in Fe-containing SPPs in commercial alloys. Corrosion studies have been performed on model alloys without Fe [20], where breakaway corrosion rate was attained with

little protectiveness of the oxide layer. Cr remains in the SPPs relatively far out in the oxide and as the particles are depleted of Fe they become amorphous [27]. Eventually Cr moves out along the basal planes in the oxide.

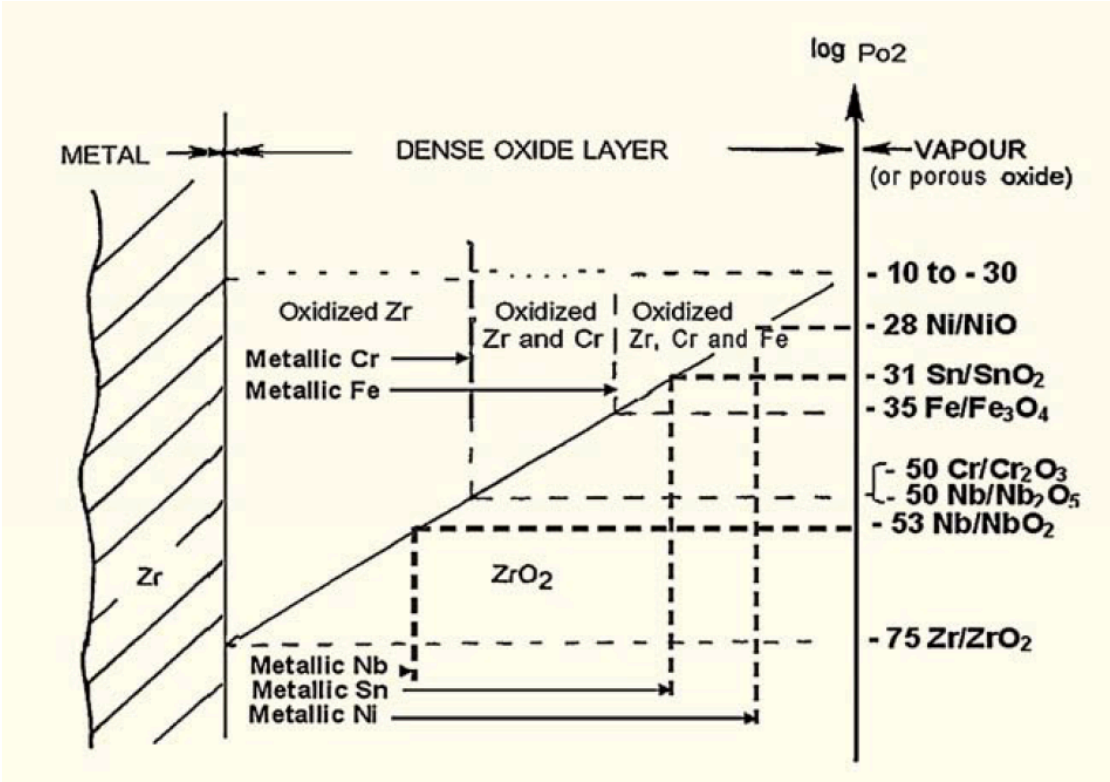

Figure 3.3: Stability diagram of alloying elements in the oxide as a function of oxygen partial pressure [28].

Similarly to Fe and Cr, nickel has very low solubility in Zr and forms SPPs with Fe. It has been suggested that the distribution of Ni in the Zr matrix is non-uniform, which could make the alloy susceptible to nodular corrosion [29]. Nickel is the most noble of the transition metal alloying elements in zirconium and can thus be expected to oxidize reasonably far out in the oxide where the partial pressure of O_2 is higher [28]. The mobility of Ni in the oxide is reportedly low, and it tends not to migrate far from the original SPP region as it oxidized [26]. It has been proposed that the delayed oxidation of precipitates may be associated with cracks and void formation in the oxide, thus reducing the protectiveness of the barrier layer [11]. The thermodynamic stability of some common alloying elements as a function of the partial pressure of O_2 is given in Figure 3.3 [28].

3.4 Irradiation effects

The fuel cladding will have little interaction with low energy thermal neutrons during operation in a nuclear reactor. However fast neutrons that have not been slowed down by the moderator will cause irradiation damage in Zr alloys. In each year of operation, each Zr atom will have been displaced on average two

times due to elastic collisions between fast neutrons and the Zr lattice [30]. One effect of the irradiation is amorphization and dissolution of precipitates [31]. Fe tends to migrate out of the SPPs in a similar fashion to the oxidation characteristics of Fe-containing precipitates. The radiation will increase the number of vacancies in the Zr crystals, resulting in accelerated diffusion. One study suggests that the electrical resistivity of the oxide film decreases upon irradiation, which may have some bearing on the electrochemistry of the corrosion process [32].

The neutron radiation in the reactor also has an impact on the mechanical properties of the cladding. Irradiation growth leads to a contraction in the *c* direction of the unit cell and expansion in the *a* directions [30]. Due to the strong texture of the fuel cladding, elongation of the tubes results, particularly at high neutron fluencies.

4. Hydrogen pickup

4.1 Overview

The overall corrosion reaction of zirconium (see section 3.1) also comprises the release of hydrogen. Some of the hydrogen that is formed in the water-splitting reaction will subsequently enter the Zr metal. To quantify this phenomenon a hydrogen pick-up fraction (HPUF) is defined as

$$HPUF = \frac{H_{absorbed}}{H_{generated}}$$

This fraction may vary greatly in different alloys and reactor conditions. The mechanisms behind the process of hydrogenation are not known, despite the fact that the problem was recognized at an early stage.

4.2 Electrochemistry

Corrosion is an electrochemical process, which is governed by a set of redox reactions. Degradation of zirconium consists of a number of possible reactions, which all can be rate determining given certain circumstances. The anodic reaction is

$$2O^{2-} + Zr \rightarrow ZrO_2 + 4e^-$$

A number of different cathodic reactions are possible such as [19]

$$2e^- + H_2O \rightarrow O^{2-} + 2H^0$$

$$2e^- + 2H^+ \rightarrow H_2$$

A water-splitting reaction may also occur at a oxide-water interface according to

$$V_O + H_2O \rightarrow O^{2-} + 2H^+$$

where V_0 is an oxygen vacancy. In most cases, the majority of the hydrogen will diffuse out in the reactor water. Interestingly, the partial pressure of H_2 dissolved in the reactor coolant appears to have little effect on the hydrogen pick-up in the fuel cladding [19]. The third reaction is therefore likely beneficial in protecting the metal from hydrogen ingress, as once protons have been reduced, the resulting H_2 can be considered inert.

The anodic and cathodic reactions need not necessarily occur at the same site, which indicates that an electron current has to be facilitated. This means that the

conductivity of the oxide is an important factor for the corrosion process. Pure ZrO_2 is a strong insulator with a band gap of 5.16 eV [33]. Reports do, however, claim that conductivity significantly improves during irradiation [34] and reactor operation [32]. This means that electrochemical considerations have to be taken when comparing autoclave and in-reactor corrosion mechanisms. Taylor proposed that the conductivity of the oxide governs where the cathodic sites for reduction are located, and suggest that an ideal oxide conductivity exists such that both oxidation rate and hydrogen pick-up can be minimized (see Figure 4.1) [35].

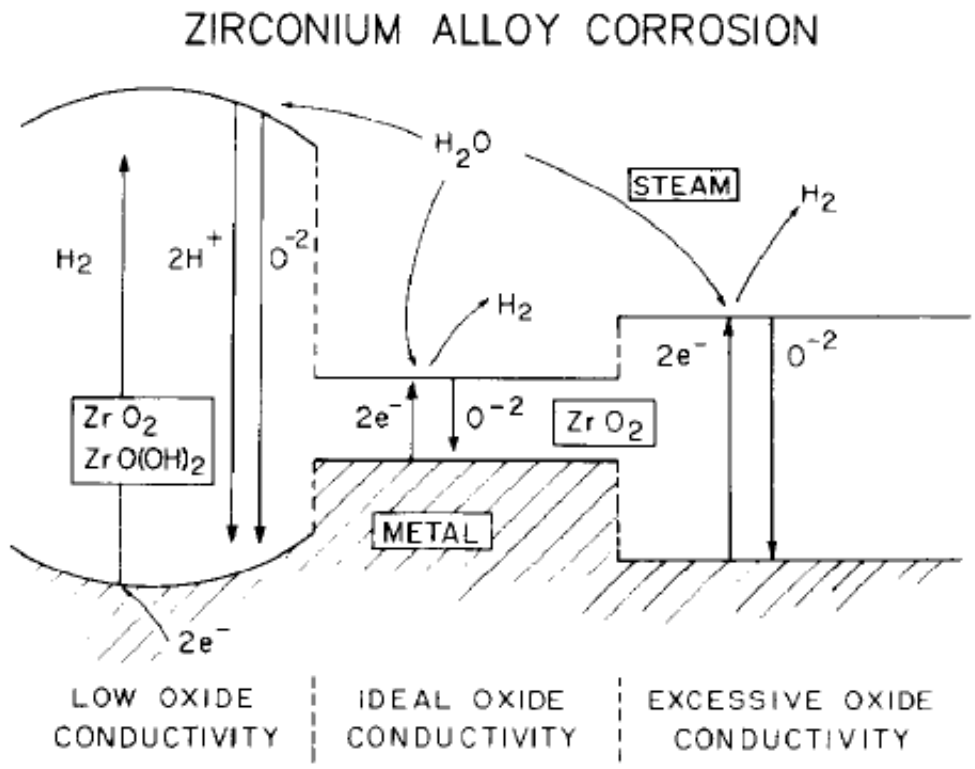

Figure 4.1: Corrosion kinetics at varying oxide conductivity, as suggested by Taylor [35].

4.3 Hydrides

Hydrogen has a relatively low solubility in α-Zr and will start precipitating as hydrides when the solubility limit is reached. The diffusivity of hydrogen in the Zr matrix is very high, which means that hydrides will not necessarily nucleate in the vicinity of the oxide but may also form in the interior of the cladding tube. The solubility is highly temperature dependent and differs significantly between operating and room temperatures. The phase diagram for Zr-H is presented in Figure 4.2 [36].

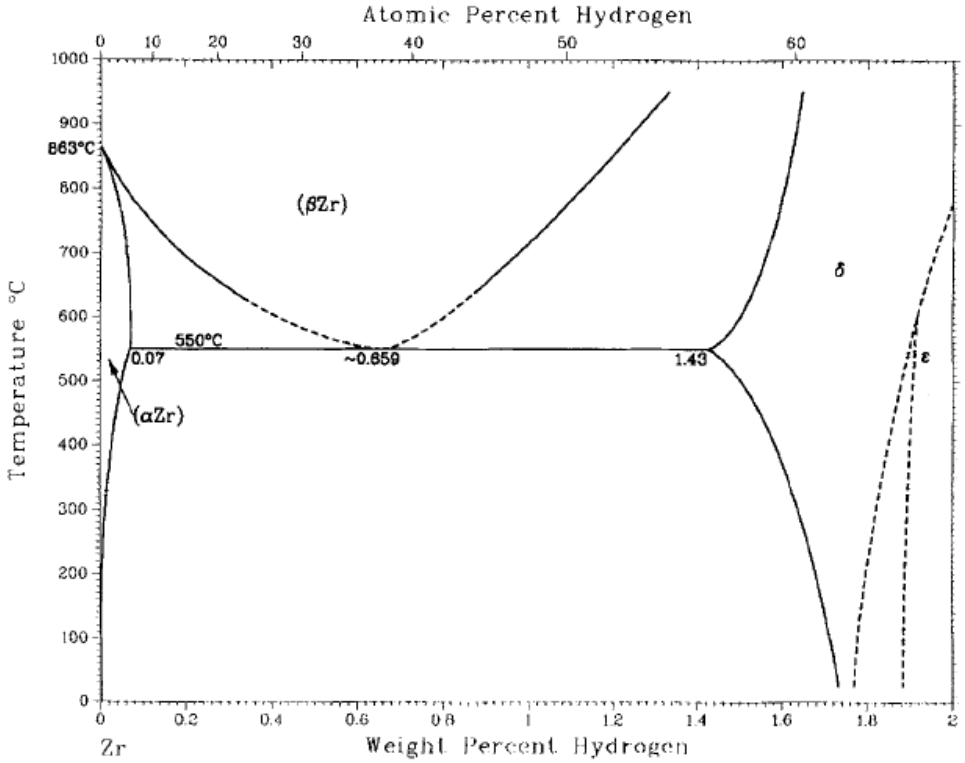

Figure 4.2: Zr-H binary phase diagram [36].

The most common hydride that is found in fuel cladding is the δ-hydride with typical stoichiometry $ZrH_{1.45\text{-}1.54}$. Some other metastable hydride phases also exist such as the γ-hydride (at high cooling rates) and the ζ-hydride, which is likely the first step of precipitation [37]. The γ-hydrides have the stoichiometry ZrH [38] and are of face centered tetragonal crystal structure. The ζ-hydride has the composition Zr_2H and is fully coherent with the α-Zr matrix [37]. At very high hydrogen concentrations, surpassing 70 atomic percent, an ε-hydride phase also exists.

The precipitation mechanism of hydrides has been studied extensively [39-41]. Upon rapid cooling or quenching the γ-hydrides form as platelets or needles parallel to the <1120> direction [40]. At lower cooling rates δ-hydrides form primarily at grain boundaries [41]. The precipitation is highly dependent on the stress situation in the tube, which is illustrated in Figure 4.3

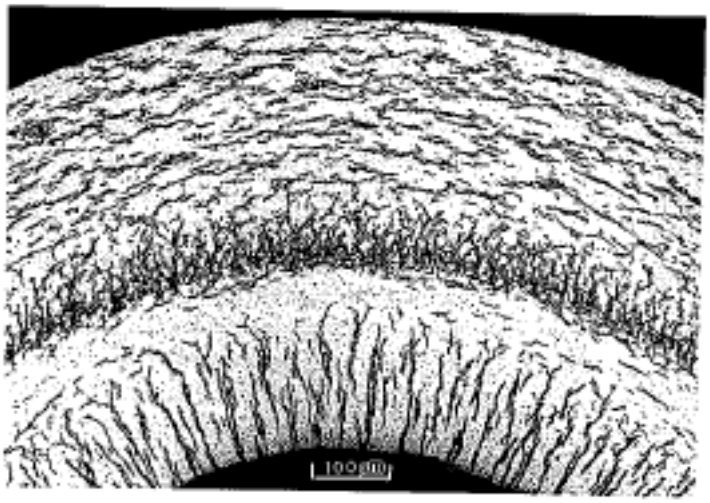

Figure 4.3: Delayed hydride cracking of a zirconium cladding tube [4]. Hydrides give dark contrast in the micrograph.

Here tensile hoop stresses, resulting from the internal pressure in the tube, have caused precipitation of hydrides in the radial direction. In the outer part of the tube hydrides precipitate in the aforementioned habit plane, characteristic of the strong crystallographic texture [4].

At low burn-ups the hydrides are typically homogenously distributed throughout the tube, and have precipitated as the tube has cooled down from reactor temperature thus reducing the solubility. At high burn-ups hydrides tend to accumulate towards the outer surface of the tube, due to the temperature gradient during reactor operation that leads to the solubility limit being exceeded earlier there [42].

4.4 Effect on material properties

Hydrogen pick-up will have a significant detrimental impact on the material properties, both in-reactor and when handling the spent fuel assemblies. In reactor, hydrogen in solution will diffuse towards areas of low temperature or higher tensile stress [4]. The first case will lead to precipitation of a hydride rim near the outer surface when the terminal solubility is exceeded. Reports suggest that these hydrides may destroy the beneficial effects of the barrier oxide layer mechanically [43,44]. The formation of the hydride rim during operation is also reported to increase the corrosion rate with a factor of approximately 1.4 [42]. Hydrogen diffusion towards areas of higher tensile stress may lead to delayed hydride cracking (DHC) of the tubes, which is a sub-critical crack growth mechanism in the material that must be avoided at any cost. DHC requires a crack in the material to be triggered, whereupon hydrogen in solution diffuses to the tip of the crack, where the stress is concentrated, and precipitates as brittle hydrides. Traces of DHC can be seen at the inner part of the tube in Figure 4.3,

which is under tensile hoop stresses leading to crack propagation outwards in the radial direction [4].

A hydride rim also has a severe detrimental effect in case of strong power transients. Such transient may be a result of what is known as RIA (reactivity initiated accident), such as fuel pellet expansion or a sudden cladding temperature increase [42].

4.5 Factors influencing HPUF

Many phenomenological studies have been carried out both in reactor and in autoclave environments. The influence of various alloying elements has been tested systematically and reported in a number of publications [45-47] (see Figure 4.4).

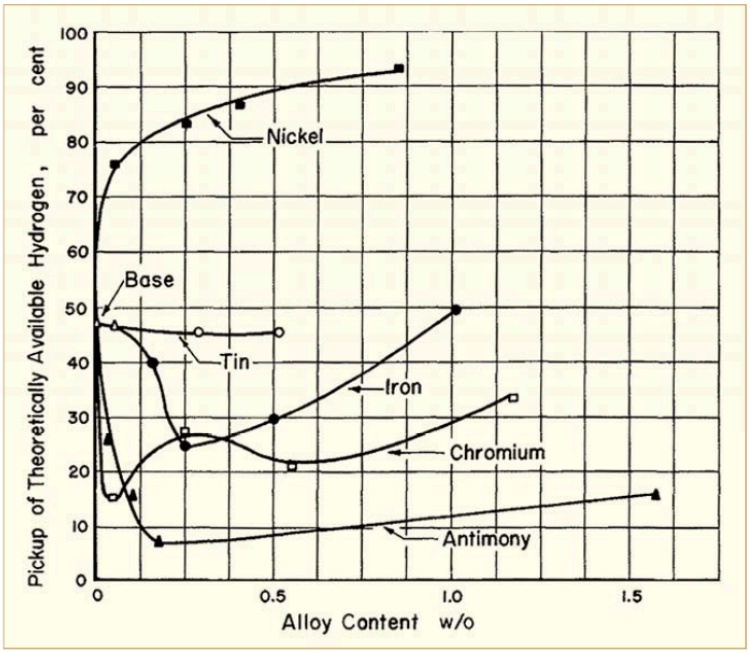

Figure 4.4: Influence of alloying elements on HPUF as measured by Berry [45].

However, a mechanistic understanding of the process, capable of explaining results from the various empirical studies has yet to emerge.

Harada and Wakamatsu report a peak in HPUF just before transition, and a sharp decline in the post-transition regime [48]. This is illustrated in Figure 4.5, and the change in HPUF is attributed to increased resistivity of the barrier layer.

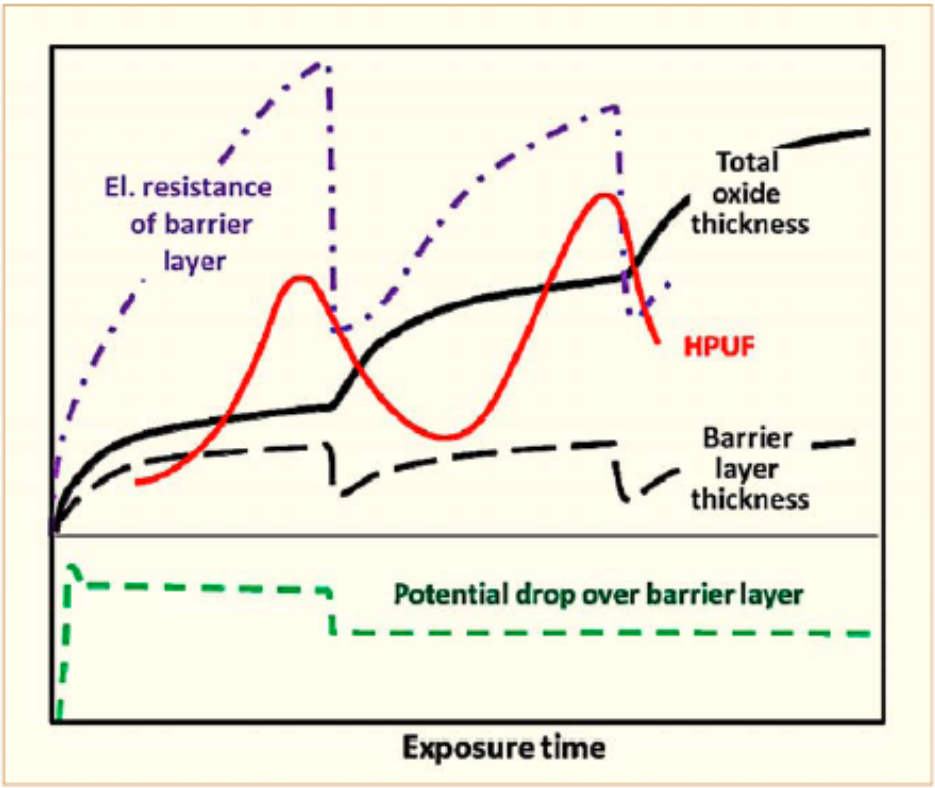

Figure 4.5: Correlation between HPUF, barrier layer thickness, total oxide thickness, electrical resistance of the barrier layer and potential drop over the barrier layer [19].

The conductivity of the barrier layer is identified as a critical factor for hydrogen pickup in other studies [49]. A conducting oxide will effectively move the cathode away from the metal, thus decreasing ingress. Kaikuchi [50] and Une [47], on the other hand, propose that hydrogen diffusivity through the barrier layer is the rate-determining step for HPUF. The reduction in HPUF in Fe containing alloys is explained by a decrease in proton mobility in the oxide due to Fe atoms in solution. Garzarolli suggests that metallic bands in the oxide grain boundaries exist, caused by segregation of alloying elements [28]. The assumption that this kind of grain boundary segregation exists in the oxide is not verified experimentally, but some speculation follows that this may lead to fast diffusion paths which may act as windows for HPU. Bossis [51] and Hatano [52] propose that SPPs in the barrier layer could be short-circuits for hydrogen uptake, and link SPPs in the oxide to the presence of hydrides in the metal underneath.

Another plausible mechanism that has been put forward [53-55] is that hydrogen traverses the oxide through microcracks and pores.

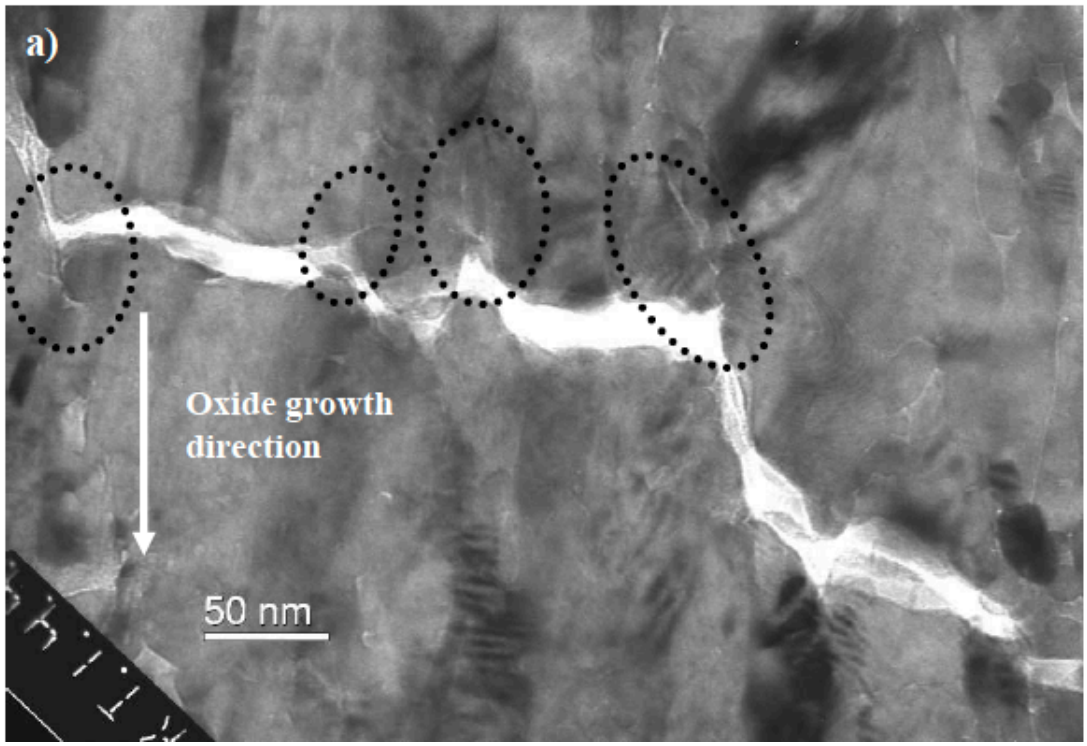

Figure 4.6: Transmission electron microscopy image of interconnected porosities and cracks in the oxide [56].

This is consistent with later TEM observations that such porosities indeed exist in the barrier layer [56] (see Figure 4.6) Networks of these interconnected pores may provide a fast route for hydrogen transport to the metal.

5. Experimental techniques

5.1 Hydrogen analysis

Being the lightest element in the periodic table, its inherent volatility makes hydrogen an extremely difficult material for microanalysis. For zirconium alloys, an abundance of different microscopy techniques have been applied over the years to investigate hydriding mechanisms. Traditional optical microscopy allows for imaging of coarse hydrides that may form in bulk zirconium, but its relatively poor resolution prohibits examination of uptake kinetics on an atomic or molecular level. Similarly, X-ray or electron diffraction techniques can yield information of hydride phases, but due to their slight size hydrogen atoms in solid solution do not affect the Zr lattice parameter to any discernable level. Energy dispersive X-ray spectroscopy (EDX) in an electron microscope has good spatial resolution, but is not sensitive to lighter elements in the periodic table and can therefore not be applied for direct hydrogen analysis. Electron energy loss spectroscopy (EELS) is suitable for hydrides, but does not suffice for detection of hydrogen in solution. Vibrational spectroscopy, such as Raman and IR, is indeed sensitive to hydrogen containing molecular complexes, but suffers from poor spatial resolution making the obtained spectra difficult to interpret. Secondary ion mass spectroscopy (SIMS) is equally sensitive to all elements, and has good spatial resolution (in ideal cases approximately 50 nm). This is a method that has been applied with some success on Zirconium alloys [Oxford-papper]. With sub-nanometer scale spatial resolution in combination with complete elemental sensitivity, atom probe tomography is a unique tool for microanalysis on the atomic level. It has successfully been used previously for microstructural examination of zirconium alloys [24, 57-61].

5.2 Atom probe tomography

5.2.1 Overview

Atom probe tomography is based on ejection of surface atoms from a needle-shaped specimen, by subjecting it to very high electric fields. The electric field, generated by a high voltage pulse applied to the specimen, will cause ionization of surface atoms of the tip, a process called field evaporation. Once ionized, the atom will be repelled by the tip and accelerated by the field toward a detector.

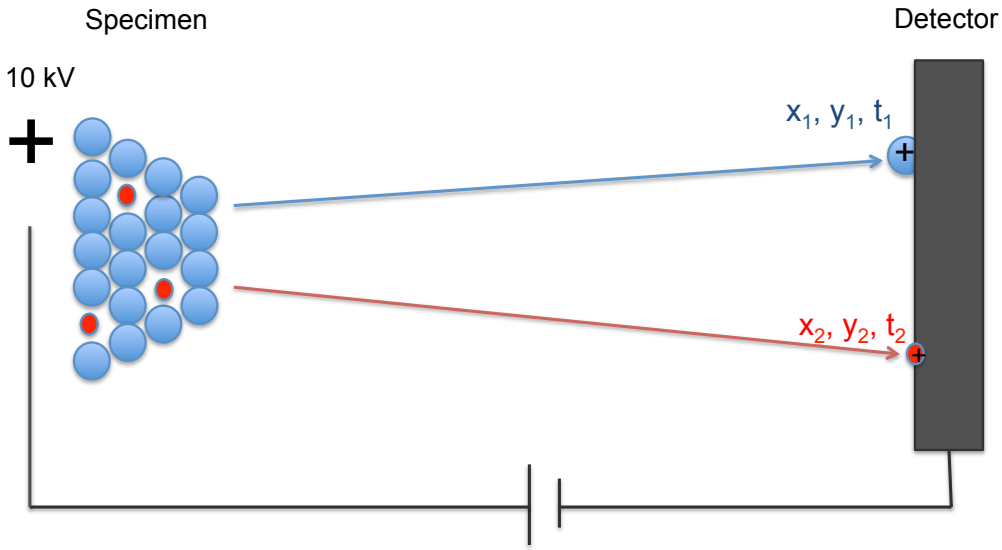

Figure 5.1: Schematic illustration of the APT analysis chamber.

Each ion that hits the detector, whether in atomic or molecular form, is registered and ascribed a time of flight (as measured from the instant of the voltage pulse) and a lateral position where it hits the detector. By assuming that only the atoms in the surface layer of the specimen are field evaporated, it is possible to evaluate their spatial position as well as atomic mass individually. This allows for reconstruction of the 3 dimensional atomic configurations in the analyzed specimen. A crude schematic illustration of the experimental setup is presented in Figure 5.1.

5.2.2 Principles of operation

For references to this section, see [62,63].

Atom probe analysis is performed in an ultra high vacuum chamber (UHV), where the pressure is held as low as possible by a system of pumps. Modern atom probes work at pressures in the 10^{-11} torr range or below. The samples are cooled to cryogenic temperatures (typically 20-100 K) in order to minimize diffusion of surface atoms, hence improving the resolution of the analysis.
Atom probe specimen must have the shape of very sharp needles, with an tip radius on the order of tens of nanometers. A high positive DC voltage, on the order of kilovolts, is then applied to the specimen in order to produce an electric field at the apex, which is slightly lower than the evaporation field of the material. The needle is mounted at a distance of approximately 40 micrometers away from a circular aperture that is held at a zero potential and serves as a counter-electrode. Clearly, a prerequisite for atom probe analysis of a material is good electrical conductivity.

Field evaporation is initiated by superimposing an additional voltage pulse on the specimen (voltage pulsed mode) or by heating the apex of the tip, using a laser beam (laser pulsed mode). These ultrashort voltage pulses (on the order of nanoseconds) will drain surface atoms of their electron density (i.e. negative charge), and cause them to ionize. The process is thermally activated and can therefore be initiated by rapid local heating of the apex by the laser pulse as well. A schematic diagram of the evaporation field dependence on temperature and field strength is presented in Figure 5.2

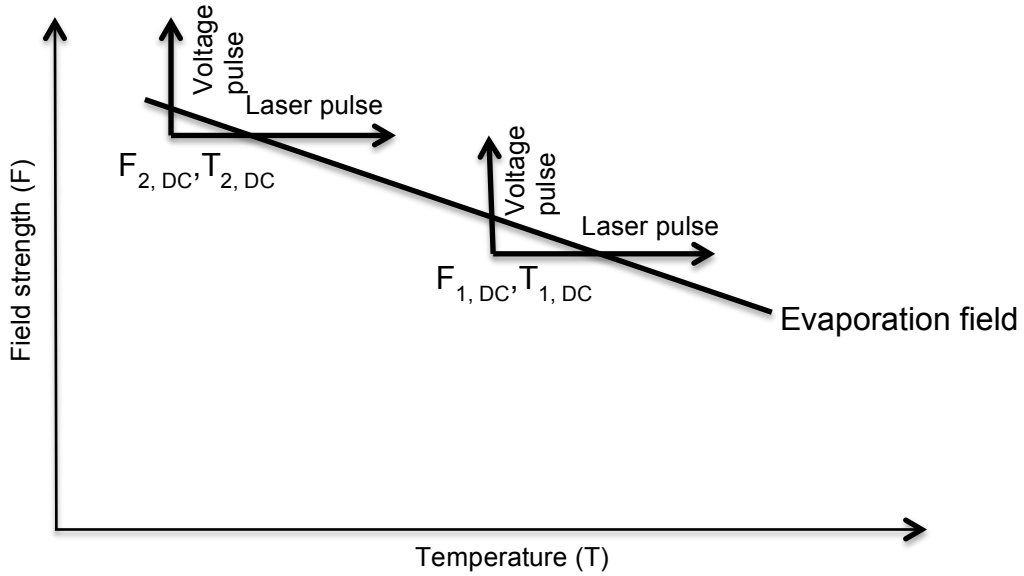

Figure 5.2: Schematic evaporation field dependence on temperature and field strength. Laser pulses are marked as horizontal arrows and voltage pulses as vertical arrows.

In a region close to the surface, atoms may also undergo additional ionization to higher charge states by electron tunneling from the ion into the specimen. This is referred to as post-ionization. The final charge state is determined solely be the magnitude of the electric field in the tip vicinity, and can be used at a later stage to estimate the field strength during analysis [64],

Once an atom has been field evaporated, thereby ionized, it is accelerated along electric field gradients away from the tip. Equaling the potential energy for the ion at the specimen surface with the kinetic energy acquired from acceleration by the electric field yields

$$n\,e\,V_0 = 1/2\,m\,d^{\,2}\,t^{\,-2}$$

where n is the charge state of the ion, e is the elementary charge, V_0 is the voltage at the tip, m is the mass of the ion, d is the distance to the detector and t is the flight time for the ion from specimen to detector. Rearranging this equation yields

$$m/n = 2\,e\,V_0\,t^{\,2}\,d^{\,-2}$$

Consequently, it is possible to correlate the measurable parameters (V_0 and t) and constants (e and d) on the right-hand side of the equation with a mass-to-charge ratio. This is the fundamental principle for mass spectroscopy, which will be discussed in more detail later on.

The APT instrument design in this study contains an energy-compensating lens – a reflectron. The reflectron is used to make corrections for energy deficits of ions that are field evaporated at a late stage of the pulse, hence not attaining the full energy $e(V_{DC}+V_{pulse})$. This is achieved by reducing the flight path length of lower energy ions through the lens, as compared with full energy ions. Thus, mass resolution of the instrument can be improved significantly.

When the ions have traversed the vacuum chamber, they are registered at a detector. The detector consists of microchannel plates and an anode. The channel plates are made of materials with high secondary electron yield, so that the ion impact will give rise to a cascade of electrons. The electrons are accelerated toward the anode where they produce a charge pulse. This charge travels in two opposite directions along a delay-line in the detector and the relative pulse delay between two or three electrodes determines where the ion has hit the detector, i.e. its lateral position.

5.2.3 Experimental factors

Although present day atom probe analysis is largely an automated process, a set of experimental parameters must be selected by the operator of the instrument. These parameters may greatly influence the outcome of the experiment as well as interpretation of the output data. Brittle materials are unsuitable for voltage pulsing due to the high stresses that are induced in the specimen by varying electric fields, and should therefore be analyzed in laser-pulsing mode.

Field evaporation of the sample is typically controlled by defining an evaporation rate for the sample. The evaporation rate is the percentage of applied pulses, voltage or laser, that will generate a hit on the detector. Once the operator has specified a rate, the software will adjust the applied voltage so as to maintain even field evaporation at this rate. Typical values are in range of 0.5-3%. Modern day atom probe instruments allow for very high pulse rates of up to 500 kHz, which means that large volumes of data can be obtained very fast.

The temperature at which the experiment is performed will influence the evaporation field of the specimen as is apparent from Figure 5.2. A high specimen temperature may induce surface diffusion on the apex of the tip, which will decrease the spatial resolution. This is particularly important during laser pulsing, where instantaneous temperature rises of hundreds of kelvin degrees may be generated for a few nanoseconds [65]. The charge states of the atoms that hit the detector are also closely related to the laser energy, as the field strength is reduced for higher temperatures. Care therefore has to be taken

when selecting laser pulse energy, so that the desired charge states are obtained and spectral overlaps are minimized.

In voltage pulsing mode, the pulse fraction, defined as V_{pulse}/V_{DC}, is another parameter that can be adjusted. If too small pulse fractions are selected, issues with field evaporation between pulses may arise. This will result in decreased detection efficiency, and also loss of data for elements with low evaporation field.

5.2.4 Data analysis

A modern day atom probe instrument has the capability to examine dimensions of up to 50x50 nm laterally and stretching up to 1 µm in the analysis direction. Such volumes contain tens or even hundreds of millions of atoms. This gives rise to vast amounts of data that requires considerable computing power to process. As described previously, each event on the detector is associated with a mass-to-charge ratio as well as three spatial coordinates. The output data is normally arranged into a mass spectrum, where the number of detector events (counts) for each mass-to charge ratio (Da) is presented. A typical mass spectrum from APT analysis of Zircaloy-2, ranging from 0-35 Da is presented if Figure 5.3

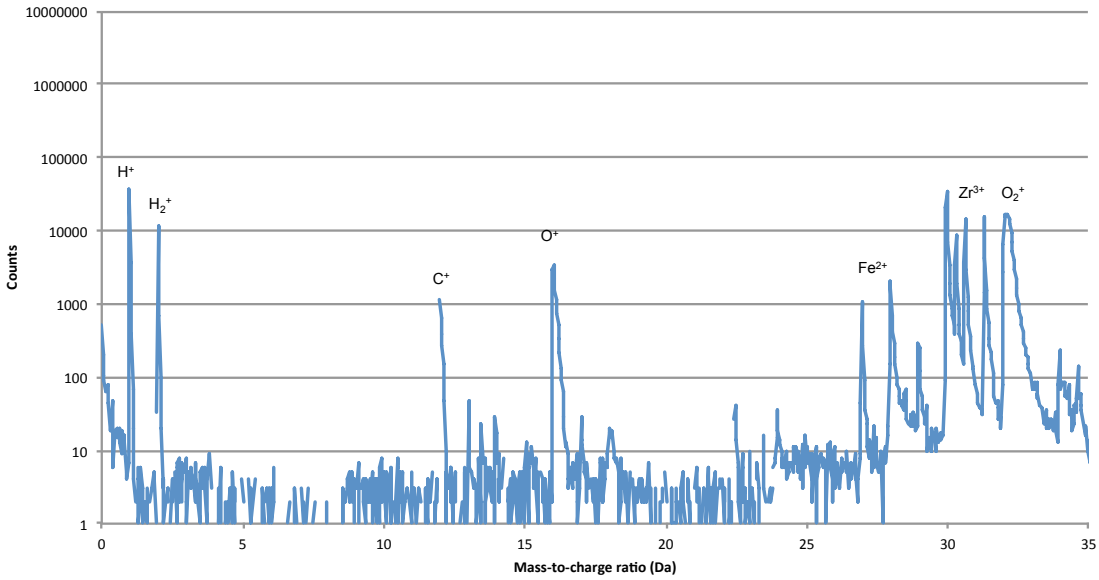

Figure 5.3: Typical mass spectrum from APT analysis of Zircaloy-2, ranging from 0-35 Da. Logarithmic scale.

Each element carries a characteristic "fingerprint" in the form of its isotope distribution. Zirconium for instance has five isotopes, where the mass distribution is 51.45% at 89.905 atomic mass units (amu), 11.22% at 90.906 amu, 17.15% at 91.905 amu, 17.38% at 93.906 amu and 2.8% at 95.908 amu. Every element in the periodic table has its own unique isotope distribution,

which, in most cases, allows for distinguishing possible overlaps between peaks that may occur in mass spectra.

Once the peaks in the mass spectrum have been evaluated and associated with a corresponding atomic or molecular species, a 3D reconstruction may be created. This permits detailed examination of the analyzed volumes, where for example information such as concentration gradients, precipitate compositions and grain boundary chemistries can be extracted through the software.

5.2.5 Limitations and artifacts

The main limiting factor for the volumes of data that can be obtained from APT is the tendency of specimen to fracture during analysis. The strong electric fields in the tip vicinity induce high stresses in the material, which may lead to rupture of the specimen. This is particularly prevalent for materials with poor conductivity, such as oxides. Therefore care has to be taken during sample preparation to ensure that the applied potential can propagate to the apex of the tip. Preparation of samples for analysis of the zirconium-zirconia system must be carried out so that the majority of the specimen consists of conducting Zr metal, with only a small scale of insulating ZrO_2 on top.

A pervading difficulty in mass spectroscopy is peak overlaps. In Zircaloy-2 a number of such overlaps exist, which must be taken into consideration to ensure accuracy in quantitative compositional analysis. One example is an isotope of the ZrO^{2+} peak at 56 Da in the spectrum, which coincides with minor alloying element Fe^{+}. To overcome this one may take advantage of the field-dependent post-ionization charge state distributions, and bring about high field strength so that most of Fe ions end up doubly charged at 28 Da.

The atomic detection efficiency in an APT instrument equipped with a reflectron is approximately 37%. This means that two-thirds of the field evaporated ions are lost and not accounted for in the data evaluation. Normally this is not a cause for great concern, as losses occur indiscriminately of element. In some cases however, certain ions evade detection and lead to erroneous compositions. Examples of this are some carbides and oxides [66, 67]

5.3 Sample preparation

5.3.1 Electropolishing

The traditional way of preparing samples for APT is an electrochemical polishing technique. It is a comparatively quick and simple method that permits multiple samples to be fabricated conveniently. In a first step a pin of approximate dimensions 0.2x0.2x20 mm is produced from the material of interest. This can be

done through various cutting or machining processes. The pin is then fastened in a sample holder and mounted in an electrochemical cell as illustrated in Figure 5.4

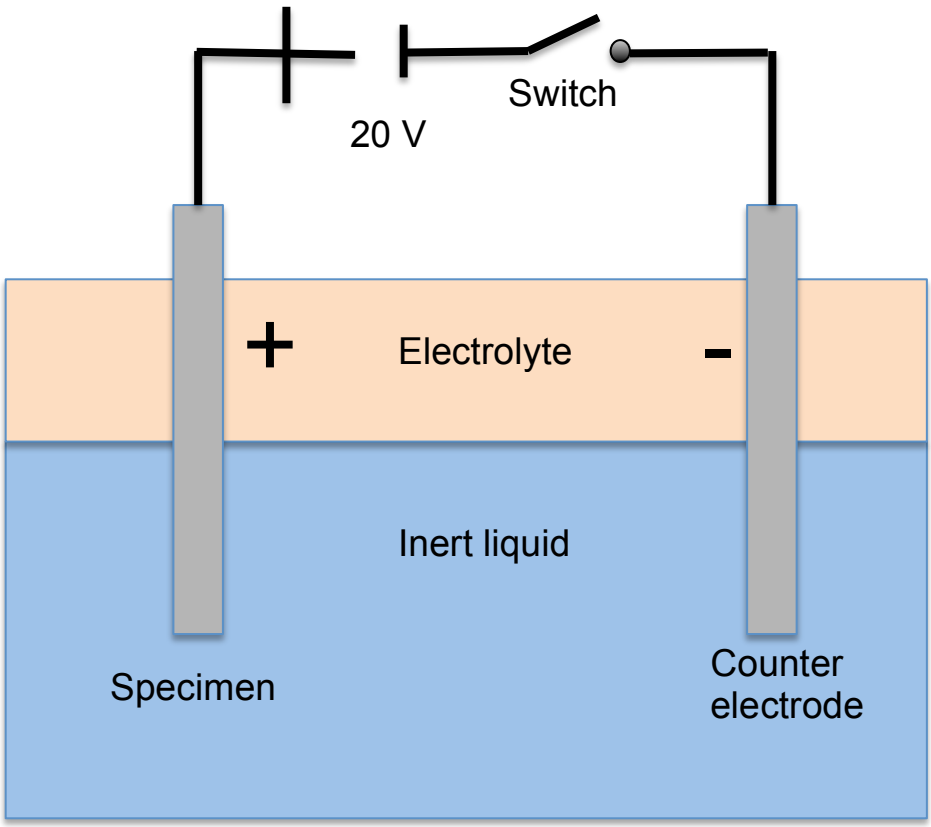

Figure 5.4: Schematics of the electrochemical cell setup during electropolishing.

A positive voltage is then applied to the specimen, where electropolishing will take place on the surface of the part of the material that is immersed in electrolyte. The electropolishing is maintained until a neck is formed on the sample. At this point, the initial electrolyte is replaced with a more dilute solution. A second electropolishing step is performed until the two ends of the pin separates and two needles are formed. This sample preparation technique is ideally suited to analysis of the bulk of materials. However if specific regions are of interest, such as precipitates, grain boundaries or phase interfaces, the electropolishing method may be inadequate as there is no way of asserting that such volumes will be included in the analysis.

5.3.2 FIB-SEM lift-out technique

The combined scanning electron microscope and focused ion beam (FIB-SEM) has opened up new possibilities in sample preparation for microanalysis, both for APT and transmission electron microscopy [68]. Scanning electron microscopes (SEM) use an electron beam that is focused through a system of electrostatic and magnetic lenses onto a specimen. Various signals are created

and can be used to analyze the sample, such as X-rays (chemical composition), backscattered electrons (atomic number contrast) and secondary electrons (topographical contrast). The focused ion beam (FIB) has a similar working principle, but the beam instead consists of ion, typically from a liquid metal source. Due to the significantly higher mass of the ions, the FIB can also be used for sputtering of material in the sample. The FIB is also equipped with an micro-manipulator needle, to which samples can be attached by deposition of platinum.

The lift-out procedure starts by deposition of a protective layer of Pt over the region of interest. Ion sputtering is then used to produce trenches at an angle of approximately 30° from the surface normal, on either side of the Pt strip. The needle is inserted into the chamber and the sample is attached onto it by Pt deposition.

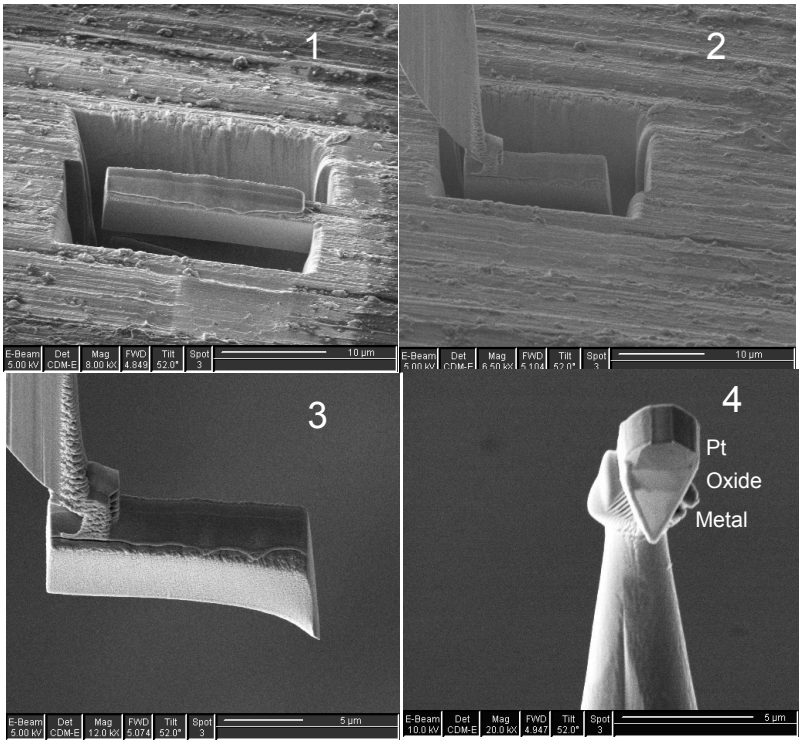

Figure 5.5: Lift-out sample preparation technique in FIB-SEM. A wedge-shaped sample is attached to a micro-manipulator needle. Slices of the wedge is then mounted on pre-fabricated Si posts**.**

Slices of the wedge-shaped specimen are subsequently attached to pre-fabricated Si posts. The procedure is depicted in Figure 5.5.

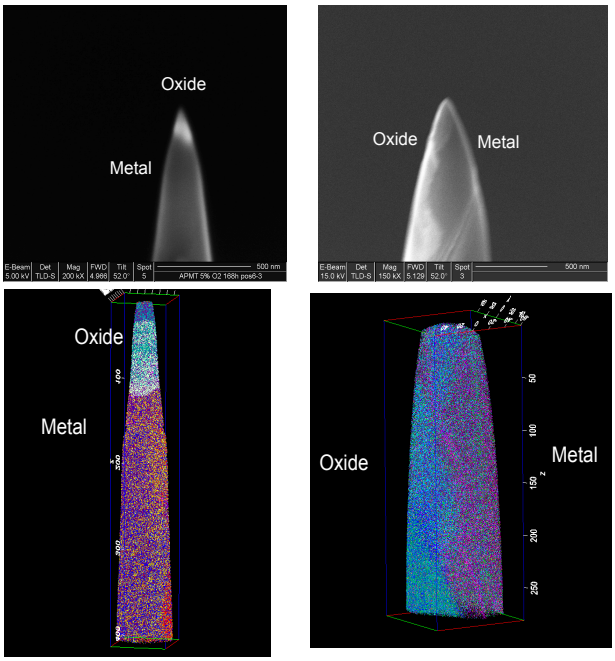

Figure 5.6: Final shape of specimen before APT analysis (above), and APT reconstructions of said specimen (below).

Once the specimen is fixed to the post, annular ion milling is performed to create a sharp needle shape where the apex is placed in the region of interest. Figure 5.6 shows two final tip shapes and the corresponding APT reconstructions.

6. Analyzed materials

6.1 Paper I

For the experiments in first paper, which is focused chiefly on method development for hydrogen analysis in APT, a material was needed that may readily withstand lengthy analysis without the risk of early fracturing. This puts the following requirements on the specimen material:

- Good conductivity
- Reasonably high strength and ductility
- Reproducible and straight-forward APT needle preparation

For these reasons an alloy containing 80% Ni, 20% Cr and small amounts of Si was selected. The name of the alloy is Nikrothal 80 and it is manufactured by Kanthal. Nickel based alloys have been analyzed since the early days of APT [Jayaram, Miller] and are known to be highly suitable for APT analysis. APT needles can readily be prepared through electropolishing of Nikrothal wires. In addition, Ni based alloys are relatively insensitive to atmospheric corrosion, which prevents the formation of an insulating oxide film at the needle surface.

6.2 Paper II

The investigated material in paper II is a tube of commercial Zircaloy-2, which is widely used for BWR applications all over the world. Due to its Ni content, Zircaloy-2 has one of the highest HPUF:s of all commercial Zr alloys, and is therefore of particular interest when studying microstructures for hydrogen uptake mechanisms. The composition of the alloy is 1.32% Sn, 0.17% Fe, 0.1% Cr and 0.05% Ni (all in weight percent). The Fe, Cr and Ni form intermetallic precipitates of compositions $Zr(Fe, Cr)_2$ and $Zr_2(Fe, Ni)$. The heat treatment employed (Westinghouse designation LK-3) gives a mean precipitate size of approximately 38 nm. A micrograph of the metal-oxide showing the precipitate distribution and the oxide scale on the material is presented in Figure 6.1.

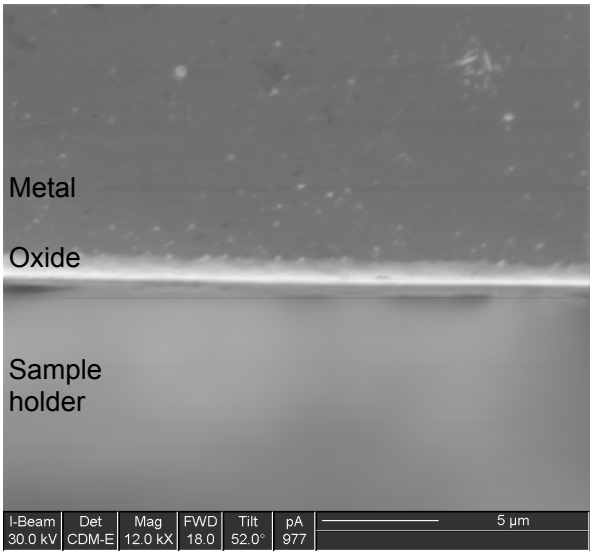

Figure 6.1: FIB-induced secondary electron micrograph of the SPP distribution and oxide scale in corroded Zircaloy-2.

The material was oxidized in steam, using a static autoclave. The pressure in the autoclave was 10.3 MPa and the temperature 400°C. The sample was kept in the autoclave for 3 days, so as to produce an oxide of thickness 1.2 µm. The weight gain of the sample is 17.8 mg/dm^2. This means that the corrosion process is in the pre-transition regime when the sample is removed from the autoclave. All material data was supplied by the manufacturer, Sandvik Materials Technology.

7. Summary of results and discussion

This work was performed as a part of the MUZIC-2 program (Mechanistic Understanding of Hydrogen Pickup in Zirconium), which is a joint project involving industry and universities aimed at gaining knowledge of the process of hydrogen pick-up in Zirconium alloys. Little work has been done to study hydrogen in APT previously, thus some groundwork in terms of method development needs to be carried out. The first paper is concerned with the adsorption mechanisms for hydrogen-containing gases is the APT vacuum chamber. This is of importance for the quantification of hydrogen content in materials, as adsorbed species will field evaporate along with the material itself and give rise to erroneously high hydrogen signal. In the second paper, the metal-oxide interface of a commercial Zircaloy-2, oxidized in steam, is examined. Previously undetected segregation of alloying elements to deformation-induced sub-grain boundaries is observed. These decorated boundaries are seen to continue interrupted into the oxide scale.

7.1 Summary of papers

7.1.1 Paper I

Experimental factors that influence hydrogen adsorption in the APT vacuum chamber are examined, with the view to allow for discrimination between residual gas and material content. We find that adsorption can be reduced either by very high field strengths, induced by voltage pulsing (applicable for analysis of Zr metal), or by field evaporation at very low field strengths, that can be achieved by laser pulsing at high pulse energies (applicable for analysis of the oxide scale). By selecting optimal analysis condition, the adsorption rate can be kept low enough (giving an apparent hydrogen concentration well below 1 at% in the analysis) to allow for some quantitative analysis of hydrogen content. Hydrogen is concluded to be supplied to the analyzed area of the tip through direct gas phase adsorption in its molecular form (H_2). It resides on the surface in the field adsorbed state from where it is subsequently desorbed through conventional field evaporation. The field strength in the tip vicinity will ultimately determine the state of the hydrogen atoms that hit the detector, i.e. the rate of dissociation of H_2^+ molecular ions. At high field strength, post-ionization of H_2^+ produces two free protons.

7.1.2 Paper II

The second paper presents previously unseen segregation in the metal-oxide interface region. The volume expansion associated with oxidation of zirconium causes deformation of the metal, and new sub-grain boundaries are formed. Fe and Ni atoms are seen to segregate to these boundaries. When the metal is

consumed by the advancing oxide front, the chemistry of the sub-grain boundaries are inherited by the oxide scale. It is not yet clear where the Fe and Ni atoms were originally located in the virgin material. Oxide grain boundaries are widely believed to be critical for the oxidation and hydriding kinetics of Zr alloys, and the observation of this segregation may contribute to a better understanding of these mechanisms.

7.2 Discussion

Based on the observations in the first paper, we are now with some confidence able to attribute the majority of the hydrogen found in the Zircaloy-2 spectra to corrosion products. A heat map of hydrogen and oxygen distributions around the metal-oxide interface in a pre-transition Zircaloy-2 is presented in Figure 7.1.

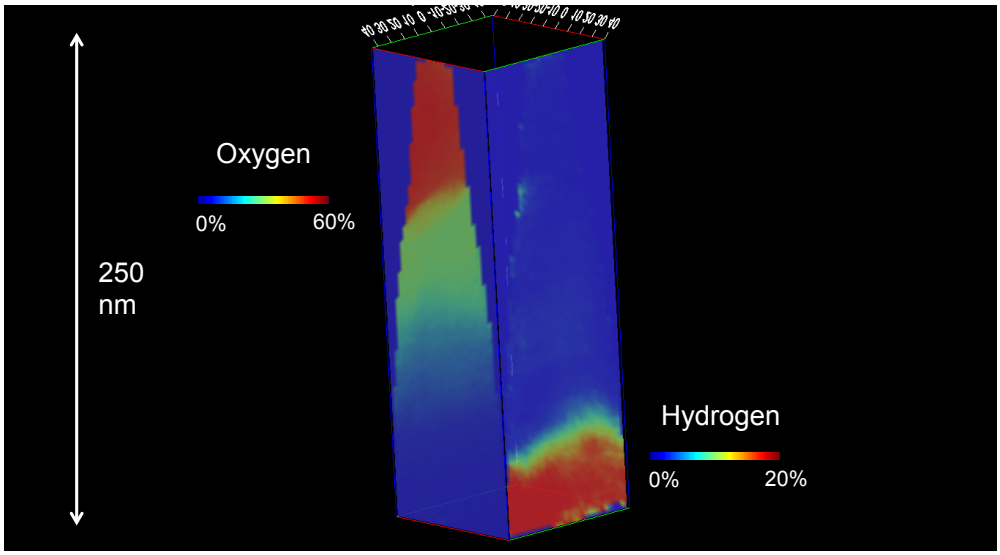

Figure 7.1: Oxygen and hydrogen heat maps from APT analysis of the metal-oxide interface region in corroded Ziracloy-2.

Hydrogen concentrations exceed 25% towards the end of the analysis, and we now have good reasons to interpret this as a hydride. Hydrogen adsorption levels from the residual gas in the vacuum chamber are never in this range, regardless of experimental conditions.

The findings in the second paper lay the foundation for a publication of more theoretical nature that has been submitted in cooperation with Prof. Itai Panas and Mikael Lindgren [69 A mechanism for hydrogen pick-up in zirconium alloys is put forward, where the oxide grain boundaries play a key role as transport paths. This is supported by density functional theory calculations, and modeling of the properties of the Fe and Ni infused oxide grain boundaries.

Acknowledgements

First of all I would like to express my gratitude to my supervisor Prof. Hans-Olof Andrén for his guidance, support and contagious enthusiasm for the subjects of atom probe tomography and zirconium corrosion. I am also very thankful for having been given the opportunity to work in this field, which I've come to enjoy immensely.

I would also like to thank my co-supervisor Dr Mattias Thuvander for countless inspiring and fruitful scientific discussions. Of course also for introducing me to everything that concerns experimental APT work; from dull electropolishing, via exciting atom probe runs to lengthy data evaluation.

Many thanks to my collaborators in the MUZIC-2 program; Prof. Itai Panas and Mikaela Lindgren at Chalmers for stimulating and thought-provoking discussions, Mats Dahlbäck, Lars Hallstadius and Maria Ivermark at Westinghouse for their scientific input at our meetings, Mattias Alm and Tomas Forsman at Sandvik and Bertil Josefsson at Vattenfall. Thanks to Haiping for keeping me in good company during project meeting travels.

The Swedish Research Council, Sandvik Materials Technology, Vattenfall, Westinghouse and EPRI are gratefully acknowledged for their financial support.

Thanks to Dr Fang Liu and Dr Leif Viskari for helping me get started on the magnificent DualBeam instrument and sharing their skills and experience.

Thanks to Dr Anders Kvist for resolving the many technical issues that arise in the lab and (impatiently) answering any questions I have, to Ola Löfgren for (patiently) assisting whenever computer problems crop up.

Thanks to my officemates during my time here Amine and Pavleta for ignoring the mess at my desk.

Thanks to the double-act Anders and Stefan (the Albert and Herbert of the fika room) for airing some shockingly dismal puns and gags, to Haiping for her heartbreaking poetry, Olof for his spiritual guidance, the Honey Aunties for their elderly wisdom, Jonatan for surrendering the badminton championship belt, Leif for his eloquent take on the English language and all the other members of the former M&M group, past and present.

Thanks to my wonderful loving parents Kickan and Gunnar for all their support and care, except for their dietary recommendations. Thanks to my prodigious brother Erik and my magnificent sister Kerstin.

References

[1] World Nuclear Association, http://www.world-nuclear.org/info/inf63.html, retrieved 2012-11-13.

[2] D.G. Franklin, P.M. Lang, *Zirconium in the Nuclear Industry 9th Int. Symp.,* ASTM STP 1132, (1991), pp. 499-535

[3] R. Adamson, F. Garzarolli, B. Cox, A. Strasser, P. Rudling, "Corrosion Mechanisms in Zirconium Alloys, IZNA7-8", A.N.T. International, (2008)

[4] R.W. Cahn, P. Haasen, E.J. Kramer, Editors, *"Materials Science and Technology – A Comprehensive Treatment, Volume 10B: Nuclear Materials Part II",* Volume Editor: B.T. Frost, Chapter 7: Zirconium Alloys in Nuclear Applications, Chapter authors: C. Lemaignan and A.T. Motta, (1994)

[5] Course material "Metallurgy and properties of Zr alloys for nuclear applications", INSTN, Chapter: Texture of Zr alloys, J.-L. Bechade, (2011)

[6] D.B. Knorr, R.M. Pelloux, "Quantitative characterization of crystallographic textures in zirconium alloys", *J. Nucl. Mater.,* Vol. 71, (1977), pp. 1-13

[7] T. Smith, *J. Electrochem. Soc.,* Vol. 112, (1969), pp. 560-567

[8] J.B. Pilling, R.E. Bedworth, *J. Inst. Met.*, Vol. 29, (1923), pp. 529-591

[9] http://www.springerimages.com/Images/Physics/1-10.1007_s11669-007-9154-2-0

[10] A.J. Motta, A. Yilmazbayhan, R.J. Comstock, J. Partezana, G.P Sabol, B. Lai, Z. Cai, *Zirconium in the Nuclear Industry 14th Int. Symp.*, ASTM STP 1467, (2005), pp. 205-232

[11] P. Tejland, M. Thuvander, H-.O. Andrén, S. Ciurea, T. Andersson, M. Dahlbäck, L. Hallstadius, *Zirconium in the Nuclear Industry 16th Int. Symp.,* ASTM STP 1529, (2011), pp. 595-619

[12] M. Parise, R. Foerch, G. Cailletaud, *J. Phys. IV France,* Vol. 9, (1999), pp. 311-320

[13] B. Hutchinson, B. Lehtinen, M. Limbäck, M. Dahlbäck, *Zirconium in the Nuclear Industry 15th Int. Symp,* ASTM STP 1505, (2009), pp. 269-284

[14] J. Godlewski, J.P. Gros, M. Lambertin, J.F. Wadier, H. Weidinger, *Zirconium in the Nuclear Industry 9th Int. Symp,* ASTM STP 1132, (1991), pp. 416-436

[15] F. Garzarolli, H. Seidel, R. Tricot, J.P. Gros, *Zirconium in the Nuclear Industry 9th Int. Symp,* ASTM STP 1132, (1991), pp. 395-415

[16] M. Preuss, P. Frankel, S. Lozano-Perez, D. Hudson, E. Polatidis, N. Ni, J. Wei, C. English, S. Storer, K.B. Chong, M. Fitzpatrick, P. Wang, J. Smith, C. Grosvenor, G. Smith, J. Sykes, B. Cottis, S. Lyon, L. Hallstadius, B. Comstock, A. Ambard, M. Blat-Yrieix, *Zirconium in the Nuclear Industry 16th Int. Symp.,* ASTM STP 1529, (2011), pp. 649-681

[17] G. David, R. Geschier, C. Roy, *J. Nucl. Mater.,* Vol. 38, (1971), pp. 329-339

[18] V. Bouineau, A. Ambard, G. Bénier, D. Pêcheur, J. Godlewski, L. Fayette, T. Duverneix, *Zirconium in the Nuclear Industry 15th Int. Symp,* ASTM STP 1505, (2009), pp. 405-429

[19] F. Garzarolli, B. Cox, P. Rudling, "Corrosion and hydriding", A.N.T. International report, (2012)

[20] A.T. Motta, M.J. Gomes Da Silva, A. Yilmazbayhan, R.J. Comstock, Z. Cai, B. Lai, *Zirconium in the Nuclear Industry 15th Int. Symp,* ASTM STP 1505, (2009), pp. 486-506

[21] Course material "Metallurgy and properties of Zr alloys for nuclear applications", INSTN, Chapter: Alloys, components and their processing, P. Barberis, (2011)

[22] M. Tupin, M. Pijolat, F. Valdivieso, M. Soustelle, *J. Nucl. Mater.* Vol. 342, (2005), pp. 108-118

[23] C.E. Coleman, R.W. Gilbert, G.J.C Carpenter, G.C Wetherly, in: *Phase Stability Under Irradiation, AIME Symp. Proc.,* J.R. Holland et al. (Eds.), Metals Park OH: Amer. Inst. Mech. Eng. (1981)

[24] B. Wadman, H.-O. Andrén, *Zirconium in the Nuclear Industry 9th Int. Symp,* ASTM STP 1132, (1991), pp. 461-475

[25] M. Ivermark, *Doctoral Thesis,* Faculty of Engineering and Physical Sciences, University of Manchester, (2009)

[26] B. Cox, H.I. Sheikh, *J. Nucl. Mater.,* Vol. 249, (1997), pp. 17-32

[27] D. Jädernäs, *"SPP dissolution and dislocations impact on in-reactor cladding behavior",* Westinghouse Zirconium Expert Group Meeting, (2010)

[28] F. Garzarolli, B. Cox, P. Rudling, *Zirconium in the Nuclear Industry 16th Int. Symp.,* ASTM STP 1529, (2011), pp. 711-728

[29] C.T Wang, C.M Eucken, R.A. Graham, *Zirconium in the Nuclear Industry 9th Int. Symp,* ASTM STP 1132, (1991), pp. 319-345

[30] Course material "Metallurgy and properties of Zr alloys for nuclear applications", INSTN, Chapter: Irradiation effects, effects on microstructure, creep and growth, F. Onimus (2011)

[31] W.J.S. Yang, R.B. Adamson, *Zirconium in the Nuclear Industry 8th Int. Symp,* ASTM STP 1023, (1989), pp. 451-477

[32] D.W. Shannon, Proc. *USAEC, Symp. On Zirconium Alloy Development,* Castlewood, CA, USA, GE Report, GEAP – 4089, Vol. II, (1962), pp. 18

[33] M. Balog, M. Schieber, M. Michman, and S. Patai, *Thin Solid Films,* Vol. 47, (1977), pp. 109-120

[34] M.M.R Howlader, C. Kinoshita, K. Shiiyama, M. Kutsuwada, M. Inagaki, *J. Nucl. Mater.,* Vol. 265, (1999), pp. 100-107

[35] D.F. Taylor, *J. Nucl. Mater.,* Vol. 184, (1991), pp. 65-77

[36] E. Zuzek, J.P. Abriata, *Bullentin of Alloy Phase Diagrams,* Vol. 11, (1990), pp. 385-395

[37] Z. Zhao, M. Blat-Yrieix, J.-P. Morniroli, A. Legris, L. Thuinet, Y. Kihn, A. Ambard, L. Legras, *Zirconium in the Nuclear Industry 15th Int. Symp,* ASTM STP 1505, (2009), pp. 29-48

[38] D.O. Northwood, *Journal of Less-Common Metals*, Vol. 48, (1976), pp. 173-175

[39] G.J.C. Carpenter, *Acta Metall.,* Vol. 26, (1978), pp. 1225-1235

[40] J.E. Bailey, *Acta Metall.,* Vol. 11, (1963), pp. 267-280

[41] J. S. Bradbrook, G.W. Lorimer, N.Ridley, *J. Nucl. Mater.,* Vol. 42, (1972), 142-160

[42] Course material "Metallurgy and properties of Zr alloys for nuclear applications", INSTN, Chapter: Impact of H Pick-up: Embrittlement, RIA, post-irradiation creep, M. Blat-Yrieix, P. Bouffioux (2011)

[43] M. Blat, D. Noel, *Zirconium in the Nuclear Industry 11th Int. Symp,* ASTM STP 1295, (1996), pp. 319-337

[44] A.M. Garde, *Zirconium in the Nuclear Industry 9th Int. Symp,* ASTM STP 1132, (1991), pp. 566-594

[45] E.B. Berry, *Corrosion,* Vol. 17, (1961), pp. 109-117

[46] B. Cox, *Advances in Corrosion Science and Technology,* Vol. 5, M.G. Fontana, R.W. Stahle (Eds.), (1976), pp. 173-391

[47] K. Une, K. Sakamoto, M. Aomi, J. Matsunaga, Y. Etoh, I. Takagi, S. Miyamura, T. Kobayashi, K. Ito, *Zirconium in the Nuclear Industry 16th Int. Symp.,* ASTM STP 1529, (2011), pp. 401-432

[48] M. Harada, R. Wakamatsu, *Zirconium in the Nuclear Industry 15th Int. Symp,* ASTM STP 1505, (2009), pp. 384-402

[49] K. Baur, F. Garzarolli, H. Ruhmann, H.-J. Sell, *Zirconium in the Nuclear Industry 12th Int. Symp,* ASTM STP 1354, (2000), pp. 836-852

[50] K.Kaikuchi, N. Itagaki, T. Furuya, A. Miyazaki, Y. Ishii, S. Suzuki, T. Terai, M. Yamawaki, *Zirconium in the Nuclear Industry 14th Int. Symp,* ASTM STP 1467, (2004), pp. 349-366

[51] P. Bossis, G. Lelièvre, P. Barberis, X. Iltis, F. Lefebvre, *Zirconium in the Nuclear Industry 12th Int. Symp,* ASTM STP 1354, (2000), pp. 918-942

[52] Y. Hatano, M. Sugisaki, K. Kitano, M. Hayashi, *Zirconium in the Nuclear Industry 12th Int. Symp,* ASTM STP 1354, (2000), pp. 901-917

[53] M.B. Elmoselhi, B.D. Warr, S. McIntyre, *Zirconium in the Nuclear Industry 10th Int. Symp,* ASTM STP 1245, (1994), pp. 62-79

[54] B. Cox, Y.M. Wong, *J. Nucl. Mater.,* Vol. 270, (1999), pp. 134-146

[55] N. Ramasubramanian, V. Perovic, M. Leger, *Zirconium in the Nuclear Industry 12th Int. Symp,* ASTM STP 1354, (2000), pp. 853-876

[56] N. Ni, "Study of Oxidation Mechanisms of Zirconium Alloys by Electron Microscopy," *Doctoral Thesis,* Department of Materials, University of Oxford, (2011)

[57] B. Wadman, H.-O. Andrén, U. Rolander, *Journal de Physique,* Vol. 49, (1988), pp. 323-327

[58] B. Wadman, H.-O. Andrén, L.K.L. Falk, *Journal de Physique,* Vol. 50, (1989), pp. 303-308

[59] B. Wadman, H.-O. Andrén, A.-L. Nyström, P. Rudling, H. Pettersson,, *J. Nucl. Mater.,* Vol. 200, (1993), pp. 207-217

[60] D. Hudson, "Zirconium Oxidation on the Atomic Scale," *Doctoral Thesis,* Department of Materials, University of Oxford, (2010)

[61] B. Gault, P.J. Felfer, M. Ivermark, H. Bergqvist, J.M. Cairney, S.P. Ringer, *Materials Letters,* Vol. 91, (2013), pp. 63–66

[62] M.K. Miller. *Atom Probe Field Ion Microscopy,* Oxford: Clarendon Press, (1996)

[63] M.K. Miller, *Atom probe tomography, analysis at the Atomic Level*, Kluwer Academic/Plenum Publishers, New York, (2000)

[64] D.R. Kingham, *Surf. Sci,* Vol. 116, (1982), pp. 273-301

[65] A. Cerezo, G.D.W. Smith, P.H. Clifton, *Appl. Phys. Lett.* Vol. 88 (2006), pp. 1-3

[66] M. Thuvander, J. Weidow, J. Angseryd, L.K.L. Falk, F. Liu, M. Sonestedt, K. Stiller, H.-O. Andrén, *Ultramicroscopy,* Vol. 111, (2011), pp. 604-608

[67] C.A. Williams, G.D.W. Smith, E.A. Marquis, *Ultramicroscopy*, In press, Available online from 27 Oct 2012.

[68] [7] D.J. Larson, D.T. Foord, A.K. Petford-Long, H. Liew, M.G. Blamire, A. Cerezo, G.D.W. Smith, *Ultramicroscopy* , Vol. 79, (1999), pp. 287–293.

[69] M. Lindgren, G. Sundell, I. Panas, L. Hallstadius, M. Thuvander, H.-O. Andrén, Submitted to *Zirconium in the Nuclear Industry 17th Int. Symp,* ASTM.